Received: 2 May 2023 | Revised: 13 December 2023 | Accepted: 16 December 2023

DOI: 10.1002/joc.8350

International Journal of Climatology | RMetS

RESEARCH ARTICLE

The 1991–2020 sea surface temperature normals

Xungang Yin[1] | Boyin Huang[1] | James A. Carton[2] | Ligang Chen[2] | Garrett Graham[3] | Chunying Liu[4] | Thomas Smith[5] | Huai-Min Zhang[1]

[1]NOAA National Centers for Environmental Information, Asheville, North Carolina, USA

[2]Department Atmospheric and Oceanic Science, University of Maryland, College Park, Maryland, USA

[3]North Carolina Institute for Climate Studies, North Carolina State University, Asheville, North Carolina, USA

[4]Riverside Technology, Inc., Asheville, North Carolina, USA

[5]NOAA Center for Satellite Applications and Research, College Park, Maryland, USA

Correspondence
Xungang Yin, NOAA National Centers for Environmental Information, Asheville, NC, USA.
Email: xungang.yin@noaa.gov

Funding information
National Oceanic and Atmospheric Administration, Grant/Award Number: NA20OAR4310339

Abstract

The 1991–2020 climate normals for sea surface temperature (SST) are computed based on the NOAA Daily Optimum Interpolation SST dataset. This is the first time that high-resolution SST normals with global coverage can be achieved in the satellite SST era. Normals are one of the fundamental parameters in describing and understanding weather and climate and provide decision-making information to industry, public, and scientific communities. This product suite includes SST mean, standard deviation, count and extreme parameters at daily, monthly, seasonal and annual time scales on 0.25° spatial grids. The main feature of the SST mean state revealed by the normals is that in the Tropics, the Indo-Pacific Ocean is dominated by the warm pool (SST ≥ 28°C) while the eastern Pacific is characterized by the cold tongue (SST ≤ 24°C); in the midlatitudes, SSTs are in zonal patterns with high meridional gradients. Daily SST standard deviations are generally small (<1.0°C) except in frontal zones (>1.5°C) mostly associated with ocean currents such as the Gulf Stream, Kuroshio and Equatorial Currents. Compared to the 1982–2011 climatology, the 1991–2020 mean SSTs increased over most global areas but obvious cooling is seen in the Southern Ocean, eastern tropical South Pacific Ocean and North Atlantic warming hole. The Indo-Pacific warm pool (IPWP) is found to have strengthened in both intensity and coverage since 1982–2011. By a count parameter criterion of ≥300 days annually with SST ≥ 28°C, the IPWP coverage increased 33% from 1982–2011 to 1991–2020. The global mean SST of 1991–2020 is warmer than that of 1982–2011, and the warming rate over 1991–2020 doubles that over 1901–2020.

KEYWORDS

1991–2020 SST normals, count parameter, extreme parameter, mean parameter, SST climatology

1 | INTRODUCTION

Climate normals are one of the fundamental parameters in describing and understanding weather and climate. They mainly serve as a benchmark or reference against which recent or current observations can be compared, and as a predictor of the conditions most likely to be experienced in a given location (WMO, 2007, 2017).

Normals are defined as period averages computed for a uniform and relatively long period comprising of at least three consecutive 10-year periods starting in a year ending with the digit 1 (WMO, 2016). Climatological standard normals were originally defined as the means of non-overlapping 30-year periods (e.g., 1901–1930, 1931–1960), with the belief that climate was essentially constant during the base periods. With the rapidly changing climate particularly since the second half of the 20th century, there was a consensus that climate reference values derived from decades ago were inadequate to represent the current climate state. Hence the World Meteorological Organization (WMO) has approved the new update frequency for climatological standard normals such that they are calculated every 10 years for the past 30-year period starting in a year ending with the digit 1 (e.g., 1981–2010, 1991–2020) (WMO, 2015). The base period for the current climatological standard normals is 1991–2020. For convenience, in the rest of the text, the term "normals" will be used to refer to "climatological standard normals," unless stated otherwise.

The concept of 30-year climate normals, first proposed by WMO's predecessor, the International Meteorological Organisation, at the 1934 Wiesbaden meeting (WMO, 2011) was initially conceived for surface meteorological elements but was gradually applied to other types of elements and also adopted by other fields particularly oceanography (WMO, 2017). However, the computation of normals for the oceans has received much less attention than for the land. The first reason is due to demand. Human beings primarily live on land and overland climate normals provide decision-making information for many activities such as travel, relocation, infrastructure design, energy pricing and crop planting. With the intensification of climate change and rapid increase of human activities over the oceans, reliable ocean climate normals have become highly desired by the industry, public and research communities. The second and key reason is due to data quality and availability. The calculation of normals requires sufficiently long and consecutive observations. Land stations with century-long weather records are common—for example, the U.S. Climate Normals included over 9800 and 15,000 stations for the 1981–2010 and 1991–2020 periods, respectively (Arguez & Applequist, 2013). In contrast, although there is a comparable history in ocean observations (Woodruff et al., 1987), fixed ocean sites with long records are rare. Ocean observations are generally taken on moving platforms, resulting in fragmentary and incomplete records. There have been several programs for stationary ocean site observations, the most significant of which being the Ocean Weather Ships (Dinsmore, 1996), established in 1948 with 13 ships located in the Atlantic Ocean, but they have gradually ended their missions since the 1970s. These observation programs can provide relatively homogeneous time series assisting long-term analysis (e.g., Taylor & Stephens, 1980) but have very limited usage in ocean climate normals as the sample size is too small for the global oceans.

In addition to station observations, area averages or points in gridded datasets are recommended by WMO as alternative formats for climate normals (WMO, 2017). By adopting various analysis algorithms, a gridding process ingests observations from one or more instruments/platforms, combines records in an area over a certain period of time and generates a dataset relatively complete in both time and space. Over land, although the station-based normals are still predominant, some countries have included gridded products in their 1991–2020 normals, such as the U.S. Climate Normals (NOAA National Centers for Environmental Information, 2022a) and the Norwegian Climate Normals (Tveito, 2021). For the oceans, the 1981–2010 sea ice monthly normals were produced over the Arctic Ocean based on gridded satellite observations (Peng et al., 2019) and the 1991–2020 ocean profile monthly climate normals on grids were developed as the World Ocean Atlas (NOAA National Centers for Environmental Information, 2022b).

The ocean regulates the global climate through its interaction with the atmosphere. Sea surface temperature (SST) is no doubt the most influential element for the air–sea interface. In the past, SST climatologies have been computed and analysed by various research groups based on gridded SST products. In the pre-satellite SST era, the gridded products used for climatology were based on in situ observations only (e.g., Bottomley et al., 1990; Shea, 1986; Shea et al., 1992). With the aforementioned issues in data quality and availability, the resolution of the early climatology products is low in both space (>1°) and time (monthly). Like the underlying input SST data, the coarse resolution climatologies have broad applications but with limitations since each grid box represents a large area on the order of ten thousand square kilometres. The large-scale representation generally means large inaccuracy and uncertainty when pointwise information is desired.

The early 1980s saw a revolutionary advance in SST development, facilitated by the satellite observations. With the five-channel Advanced Very High Resolution Radiometers (AVHRR) equipped on NOAA-7 launched in June 1981 (Minnett et al., 2019), high-resolution satellite SSTs became available. In situ and remote sensing observations together have made a huge difference for SST measurements: while the former provides ground truth, the latter expands the spatiotemporal coverage tremendously. The satellite or blended satellite-in situ products can produce daily SSTs on much finer spatial scales

with full global coverage, which enables SST climatology to be produced at daily scales with more accurate spatial representations. Based on the NOAA Daily Optimum Interpolation SST (DOISST) (Reynolds et al., 2007), Banzon et al. (2014) computed the 1982–2011 daily mean SST climatology. Since 1982 is the first full year in which satellite SSTs were available, the 1991–2020 SST climatology signifies the first high-resolution climatological standard normals that can be derived for SSTs.

The goal of this paper is to document the procedures used to produce the 1991–2020 SST normals and compare certain parameters with those from the 1982–2011 climatology. The rest of the paper is organized as follows. Section 2 presents the data and methods for the computation of 1991–2020 SST normals. Section 3 exhibits the normals by selected parameters. In section 4, we show comparisons between the 1991–2020 and the 1982–2011 climatologies. Summary and discussions are given in section 5.

2 | DATA AND METHODS

2.1 | Data

The NOAA Daily Optimum Interpolation SST, version 2.1, dataset (DOISST v2.1) (Huang et al., 2021a) is used for computing the 1991–2020 SST normals. The DOISST is a blend of in situ observations and satellite SSTs derived from AVHRR, analysed on 0.25 latitude–longitude grids with full global coverage for oceans and large lakes. The data are available since September 1981 and updated daily. The 1982–2011 climatology (Banzon et al., 2014) was computed from the previous version of DOISST, v2.0 (Reynolds et al., 2007), but the underlying input data remain the same in the current version of DOISST. The update from version 2.0–2.1 only impacts the SSTs since 2016, primarily due to changes in satellite and in situ data inputs, bias correction, and sea ice temperature algorithm (Huang et al., 2021a).

The DOISST makes a compromise between the much higher resolution of satellite data and the much lower resolution of in situ data. Its 0.25° spatial resolution, which is on the coarser end of the spectrum of satellite SST products, may not be able to resolve all the smaller submesoscale eddies. Huang et al. (2023) made a comparison of SST products that were all gridded on the same 0.25° resolution and concluded that DOISST has good performance scores from 2016 to 2022. In contrast, Yang et al. (2021) found that the DOISST was cold biased from the ensemble mean during the 1982–2002 period. We recognize that the difference among SST products may impact the computed SST normals. Given the relatively small magnitude of the difference among SST products and the relatively lower variability over the ocean, DOISST should be sufficient to provide reliable SST normals information to most of the needs of users.

Two supporting data sets are used in this study: The monthly 2° × 2° SSTs from the Extended Reconstructed SST (ERSST) version 5 (Huang et al., 2017) and the monthly 0.25° × 0.25° meridional wind at 10 m (v-wind) from the European Centre for Medium-Range Weather Forecasts (ECMWF) Reanalysis v5 (ERA5; Hersbach et al., 2020). ERSST is a global monthly SST data set derived from in situ observations. It is produced on grids with spatial completeness enhanced using statistical methods. ERSST begins in January 1854 continuing to the present. ERA5 is the fifth generation ECMWF atmospheric reanalysis of the global climate, covering the period from January 1940 to present. It provides a large number of atmospheric, land and oceanic variables in different spatiotemporal resolutions.

2.2 | Methods

Based on the WMO guidelines (WMO, 2017) with some modifications to the original definitions, the principal (mean) and secondary (count and extreme) climatological parameters are computed at selected time scales using the DOISST (Table 1). Standard deviations (SDs) for the SSTs during the averaging period are also computed as part of the principal category. It is to be noted that although the daily normal is not currently required by WMO, it certainly provides important information that is missing in the longer-time scale parameters and it is becoming more popular in member countries (WMO, 2018).

2.2.1 | Principal climatological parameters

In this category, daily, monthly, seasonal and annual SST 30-year mean parameters and SDs are computed.

Daily SST mean parameter

A straightforward method to calculate the daily normal SST for a given day at a site (grid) is to take the arithmetic mean of all the SSTs during the averaging period (1991–2020) for the day in question,

$$Y_i = \frac{1}{N}\sum_{n=1}^{N} Y_{i,n}, \quad (1)$$

where $i = 1, 2, \ldots, 365$ is the Julian day of a year without considering leap years; N is the total number of years in the averaging period, which is 30 for the 30-year normals;

TABLE 1 Climatological parameters computed for the 1991–2020 SST normals.

Category	Type	Parameter	Units	Daily	Monthly	Seasonal	Annual
Principal	Mean	Mean SST (and standard deviation)	°C	✓	✓	✓	✓
Secondary	Count	Mean No. of days with SST ≥ 16, 17, ..., 34°C	Count		✓	✓	✓
		Mean No. of days with SST = −1.8°C, <0, 1, ..., 15°C	Count		✓	✓	✓
	Extreme	Highest recorded values of daily SST	°C		✓	✓	✓
		Lowest recorded values of daily SST	°C		✓	✓	✓

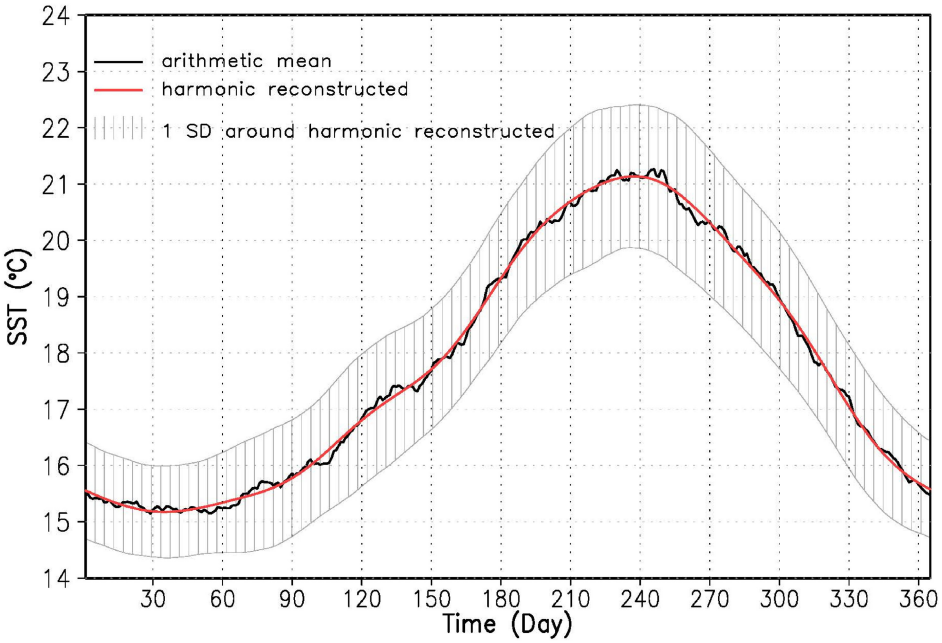

FIGURE 1 Daily normal SSTs (units: °C) computed by arithmetic mean (black line) and six-harmonic reconstruction (red line) in a grid box centred at (32.625°N, 117.375°W). The hatched area is one standard deviation (SD, units: °C) around the harmonic reconstructed normal SSTs. [Colour figure can be viewed at wileyonlinelibrary.com]

$Y_{i,n}$ is the gridded SST data from DOISST in Julian day i of year n; and Y_i is the daily normal SST computed by arithmetic mean for Julian day i of the year.

However, due to the limited sample size ($N = 30$), daily means computed by Equation (1) more likely contain considerable high-frequency noises of meteorological, observational and instrumental origins. For example, in Figure 1, the black line shows the 1991–2020 daily SST means calculated by arithmetic mean method for the grid box centred at (32.625°N, 117.375°W), about 20 km off the southern California shore. Apparently, the curve with wiggles is counterintuitive for daily normal SST since a smooth curve primarily reflecting seasonal variations is expected in this case. To achieve the statistically and climatologically meaningful normals for daily SST, it is essential to remove the noises.

Harmonic analysis, which detects regular periodic signals, is one of the commonly used smoothing techniques in the computation of climate normals (Epstein, 1991; von Storch & Zwiers, 1999; Wilks, 2006). For the daily mean parameter, we use a certain number of low-frequency harmonics, neglecting the rest of the harmonics which can be considered as high-frequency noises, to reconstruct a time series representing the "true" climatology. Let $\overline{Y_i}$ be the harmonic reconstructed value of the arithmetic mean value Y_i in the day i, determined by the first k harmonics,

$$\overline{Y_i} = a_0 + \sum_{j=1}^{k} \left[a_j \cos(2\pi ij/T) + b_j \sin(2\pi ij/T) \right], \quad (2)$$

$$a_0 = \frac{1}{T} \sum_{i=1}^{T} Y_i, \quad (3)$$

$$a_j = \frac{2}{T} \sum_{i=1}^{T} Y_i \cos(2\pi ij/T), \quad (4)$$

$$b_j = \frac{2}{T} \sum_{i=1}^{T} Y_i \sin(2\pi ij/T), \quad (5)$$

where $T = 365$ is the total number of days in a year. February 29th, which appears only in leap years, is excluded in harmonic analysis to avoid the likely inconsistency in the time series due to its much smaller sample size for the mean. In the final product of SST normals,

the value for February 29th will be inserted by the average of February 28th and March 1st values.

The number of harmonic components k can be selected is between 1 and $T/2$, while too small (or too large) would result in underfitting (or overfitting). Based on the analysis of 198 U.S. land stations, Epstein (1991) showed that for 5-day mean temperatures, the selection of 2–5 harmonics were all acceptable and claimed that the conclusion should be also applied to daily temperatures. However, both the analyses by Arguez and Applequist (2013) for land station temperatures and by Banzon et al. (2014) for gridded SSTs concluded that six harmonics were adequate for smoothing daily temperature means. In this work, we adopt the conclusion reached by the latter two studies, using six harmonics ($k = 6$ in Equation (2)) to reconstruct the daily normal SSTs. The analysis of Banzon et al. (2014) indicated that the first six modes can explain about 99% of the total variability and more added modes only benefit low-standard deviation areas between 10°S and 10°N and north of 80°N and therefore the actual added signal would be very small. For the example displayed in Figure 1, the six-harmonic smoothing result is shown by the red line. As we can see, the high-frequency noises in the arithmetic mean SSTs have been effectively removed by the harmonic approach, resulting in a smooth curve for the daily normal SSTs.

Monthly, seasonal and annual SST mean parameters

Monthly normal SSTs are computed directly from the daily normal SSTs. For a given month, the normal value is the arithmetic mean of the daily normals during the month. For February, only 28 days (Days 1–28) are used.

Seasonal and annual normal SSTs are computed from monthly normals. The four seasons are defined as boreal winter (January–February–March [JFM], spring (April–May–June [AMJ]), summer (July–August–September [JAS]) and fall (October–November–December [OND]). The four seasons are defined based on the SST climatology which shows that the 3-month average SST in the Northern (Southern) Hemisphere is the lowest (highest) in JFM and highest (lowest) in JAS. The seasonal normal value for a given season is the arithmetic mean of the monthly normals for the seasons concerned; and the annual normal value is the arithmetic mean of the 12 monthly normals. As recommended by WMO (2017), all months are treated equally in the computation of seasonal and annual SST mean parameters without weighing the number of days in each month.

Standard deviation

For an SST mean parameter at time i ($i = 1, 2, ..., 365$ for daily; $i = 1, 2, ..., 12$ for monthly; $i = 1, 2, 3, 4$ for seasonal; or $i = 1$ for annual), the SD s_i during the averaging period is computed in reference to the corresponding normal SST value $\overline{Y_i}$,

$$s_i = \sqrt{\frac{1}{N-1}\sum_{n=1}^{N}\left(Y_{i,n} - \overline{Y_i}\right)^2}, \tag{6}$$

where N is the total number of years and $n = 1, 2, ..., N$ is each year during the averaging period. For the daily SST SDs, a centred 29-day equal-weight smoothing is applied to remove the high-frequency variations. In the example of daily normals shown in Figure 1, one SD around the harmonic reconstructed values (red line) is shown as the hatched area.

2.2.2 | Secondary climatological parameters

In this category, SST count and extreme parameters are derived for monthly, seasonal and annual time spans. The monthly count values are calculated directly from the input SST data, while the seasonal and annual count values are derived from the monthly count values. In the WMO guideline, count parameters are based on the maximum and minimum temperatures, which are routinely reported by land stations but unavailable in the gridded daily SSTs. However, SSTs have small diurnal ranges, generally less than one degree (Kawai & Wada, 2007; Stuart-Menteth et al., 2003), which means that the difference among the maximum, minimum and daily mean SSTs is small. In comparison, the overland diurnal temperature ranges can be more than 10 degrees on average (Wang & Clow, 2020). Therefore, for the SST, we simply use the daily mean data to compute the count parameter.

Based on the daily SST input data during the averaging period, the following count and extreme parameters are computed for each of the 12 months: mean number of days with SST ≥ 16, 17, ..., 34°C; mean number of days with SST = −1.8°C, <0, 1, ..., 15°C; and highest and lowest recorded values of SST. For the two count parameters, the monthly values are calculated by weighing the number of days in each month during the averaging period for the month in question. This is done by first computing the count ratio for each month during the averaging period, and then the monthly count is derived by multiplying the average number of days of the month by the mean of all the monthly count ratios during the averaging period for the month in question. In fact, the use of weight only affects February since this is the only calendar month with varying number of days. There are eight leap years during 1991–2020 and thus the average number of days for February is 28 + 8/30 = 28.27. With the monthly count parameter computed, the seasonal and annual count values are derived as the sum of the

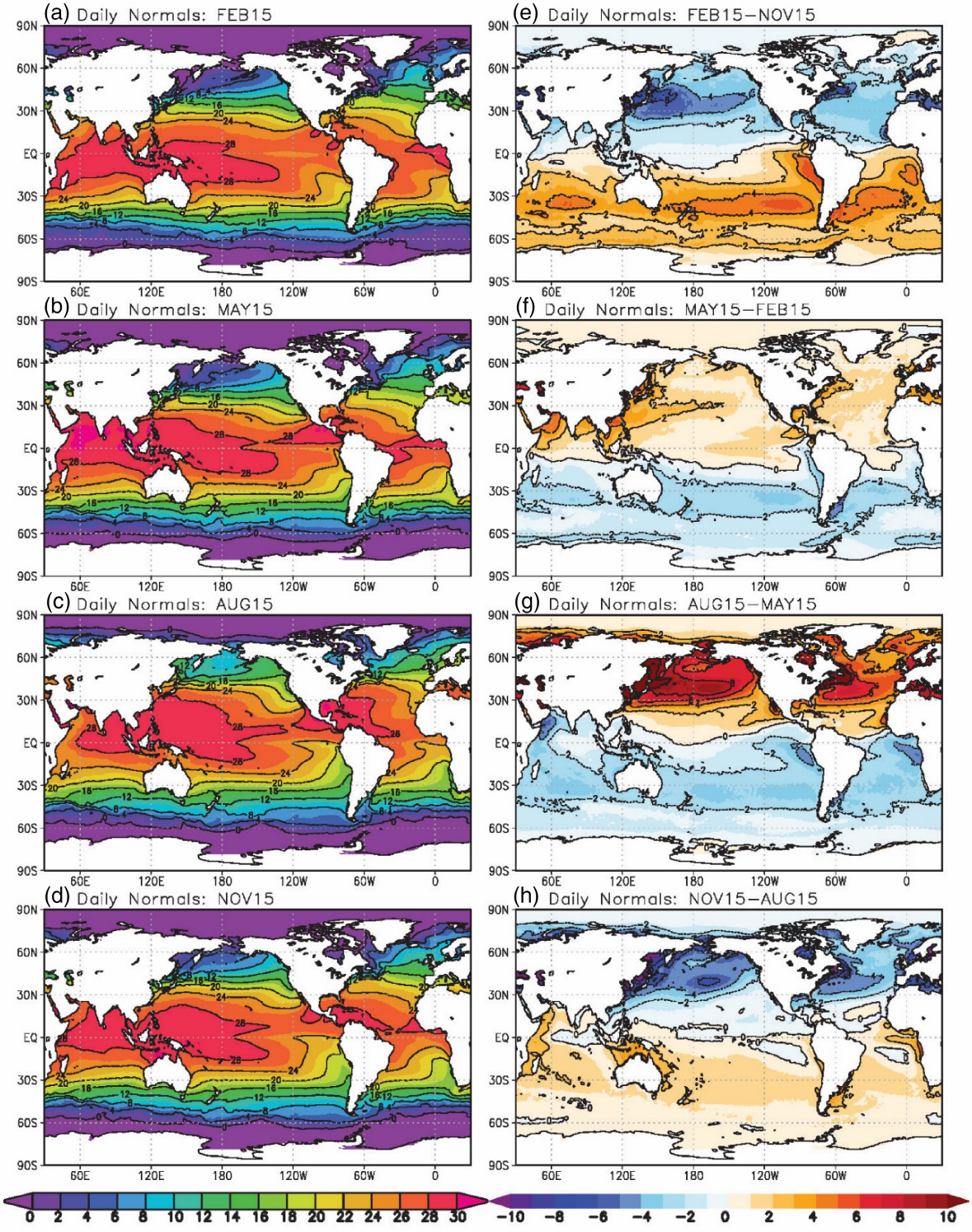

FIGURE 2 Daily normal SSTs and seasonal differences (units: °C) for the middle days of the four seasons. The left column shows the four daily maps: (a) Feb 15, (b) May 15, (c) Aug 15 and (d) Nov 15. The right column shows the difference between each day and the day in the previous season: (e) Feb 15–Nov 15, (f) May 15–Feb 15, (g) Aug 15–May 15 and (h) Nov 15–Aug 15. [Colour figure can be viewed at wileyonlinelibrary.com]

monthly count values for the months concerned. For the extreme parameters, seasonal and annual values are the highest/lowest of the values for the months concerned.

3 | RESULTS

In this section, the 1991–2020 SST normals are presented by selected examples from each normals category.

3.1 | Principal climatological parameters

The left column of Figure 2 shows the daily normal SSTs from 4 days which are, respectively, the middle day of each season so they are also used here to represent the mean states of seasonal SSTs. These are general SST patterns that have already been described in many books and articles (e.g., Emery, 2015; Minnett et al., 2019; Talley et al., 2011), but in this paper we present them in terms of SST normals and their seasonal variations (right column of Figure 2), which are represented by the differences between each of the 4 days and the day in the previous season. Overall, SSTs are higher in the Tropics and decrease poleward, with SST values ranging from over 28°C to freezing point. In the midlatitudes of both the Northern Hemisphere (NH) and Southern Hemisphere (SH), particularly the latter, SSTs are dominated by zonal distribution patterns in all seasons with high meridional gradients as reflected by the dense isotherms. From season to season, the isotherms periodically move northward from boreal winter to summer and then southward from summer to winter. The meridional tilting of the isotherms in the seas off the coasts of continents reflects the influence of ocean currents. For example, north of 45°N in the Pacific, while the Oyashio pushes cold water southward in the west, the Alaska current transports warm water northward in the east, resulting in southwest–northeast inclined isotherms. In contrast, the isotherms in the tropical oceans are much less dense but a striking feature in the tropical oceans is the extensive coverage of the warm pool SSTs exceeding 28°C. The warm pool is seen in all oceans during all seasons, but is most pronounced in the Indo-Pacific Oceans with coverage from the western Indian Ocean to the central Pacific Ocean. The Indo-Pacific warm pool (IPWP) is stronger during the boreal spring and summer seasons: in the spring (Figure 2b), the warm pool in the Indian Ocean situates north of approximately 10°S where SSTs exceed 30°C in the Arabian Sea, Bay of Bengal and seas around Southeast Asia; during the summer (Figure 2c), although the portion of the warm pool in the Indian Ocean becomes the weakest of all seasons, the portion in the Pacific Ocean reaches its strongest phase with the highest meridional extent beyond 30°N in the western boundary. In contrast to the existence of the warm pool in the west, the cold tongue, as outlined by the 24°C isotherms, exists in the eastern tropical Pacific in all seasons and is more evident during the boreal summer and fall seasons (Figure 2c,d).

In general, season-to-season changes of normal SSTs (Figure 2e–h) are small in the topical and SH oceans, mostly less than 2°C and rarely above 4°C, but large in the midlatitude North Pacific and North Atlantic Oceans, often between 4 and 8°C during the boreal spring–summer–fall–winter transitions (Figure 2g,h,e). In the Arctic Ocean, due to seasonal ice coverage changes, the seasonal variation is low (<2°C) during boreal fall–winter–spring (Figure 2a,b) cold seasons, but can reach 4°C during boreal spring–summer–fall (Figure 2g,h) warm seasons in the southern Arctic Ocean. In the midlatitude oceans, the winter to spring SST variation (Figure 2f for NH and Figure 2h for SH) is nearly uniformly below 2°C except in the coastal areas, while the spring to summer SST change is the highest for each hemisphere: 2–6°C for SH (Figure 2a) and 4–10°C for NH (Figure 2g). The highest seasonal variations (over 10°C) are mostly found along the Kuroshio and Gulf Stream during the boreal spring–summer–fall seasons (Figure 2g,h).

Figure 3 presents the global distribution of annual normal SST (left panel) and the zonal means for both the annual and the four seasonal normal SSTs (right panel). The general distribution of the annual SST is similar to that of the daily SSTs shown in Figure 2 but in a much smoother fashion. From both panels we can see that the normal SSTs poleward of 75°N in the Arctic Ocean and 60°S in the Southern Ocean are mostly below 0°C and are close or at the freezing point toward the two poles. In the Tropics except part of the seas off the west coasts under the influence of eastern boundary currents, SSTs are above 20°C but rarely above 30°C. Throughout the year, as shown in both Figures 2 and 3, the Indo-Pacific Ocean is the warmest region dominated by warm pool temperatures exceeding 28°C. The highest meridional SST gradients are found in the midlatitudes of both hemispheres, with more than a half-degree temperature change per degree latitude change on average. The global mean annual normal SST is 18.2°C.

The zonal means (Figure 3, right panel) reveal two features in SST normals: (1) As a consequence of the cold tongue in the eastern tropical Pacific just south of the Equator, the equatorial zone is slightly cooler than its bordering zones; the global highest SST zone is a few degrees north of the Equator; (2) seasonal shifts of isotherms in the NH are much larger than in the SH; in the midlatitude to high latitude, seasonal movements of the isotherm are minor in the SH but the highest in the NH, approximately between 45 and 70°N latitude bands with SSTs between 5 and 10°C.

Daily SST SDs in reference to daily normal SST values during 1991–2020 are less than 1°C in the majority of the global oceans, as shown in Figure 4. Areas standing out with year-round large SDs (>1.5°C) are generally associated with oceanic currents/fronts such as the western boundary currents (e.g., Kuroshio, Gulf Stream, Agulhas and Brazil Currents); coastal upwelling fronts off the west coasts of North America, South America and Africa; the equatorial upwelling front in the equatorial eastern

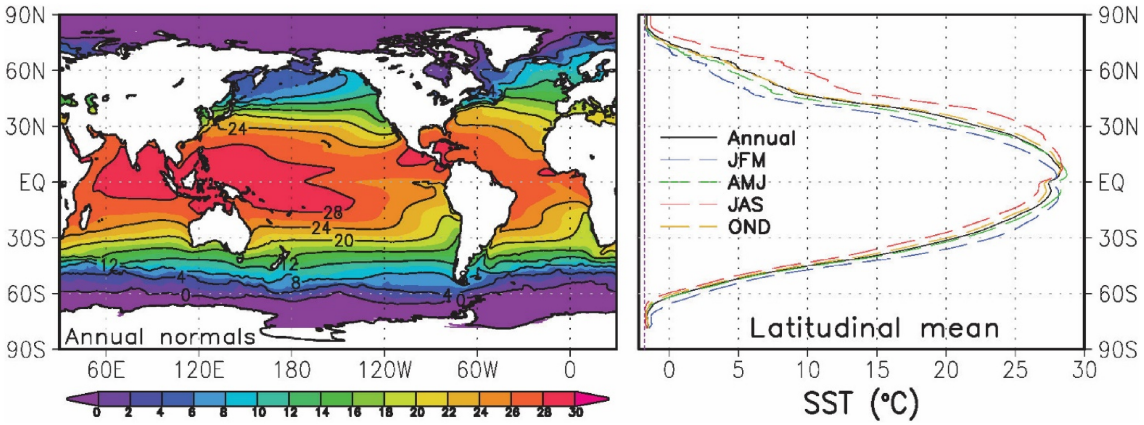

FIGURE 3 Annual normal SST (units: °C) pattern (left panel) and the zonal means of annual/seasonal normal SST (right panel). [Colour figure can be viewed at wileyonlinelibrary.com]

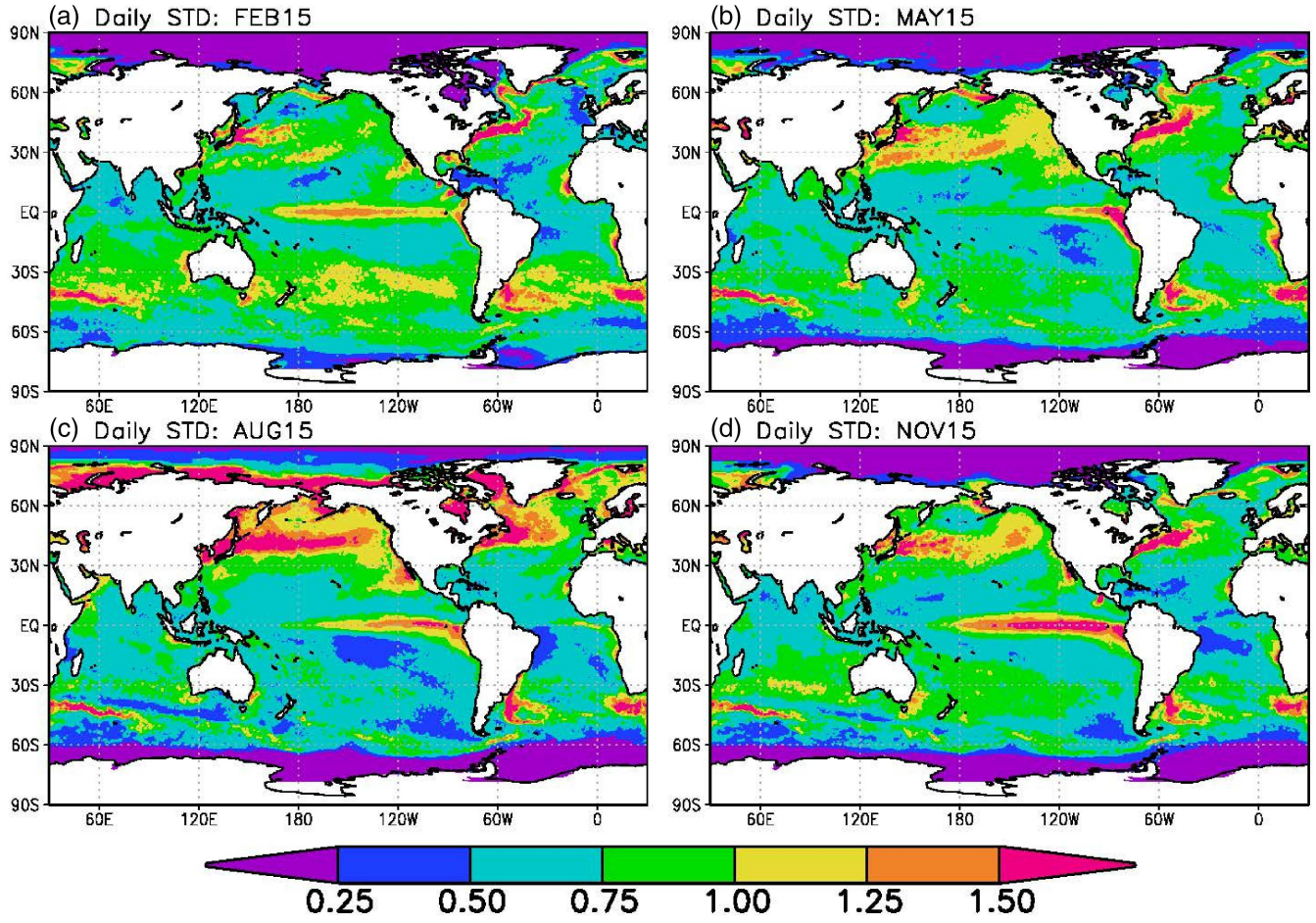

FIGURE 4 Daily SST SDs (units: °C) with respect to daily normal SSTs for the middle day of each season: (a) Feb 15, (b) May 15, (c) Aug 15 and (d) Nov 15. [Colour figure can be viewed at wileyonlinelibrary.com]

Pacific; and the East Greenland Current located to the west and south of Greenland. The seasonal changes of SDs in the equatorial eastern Pacific Ocean also reflect the ENSO events, which commonly develop in boreal spring and reach peaks in the fall to winter.

In the midlatitude and high latitude, particularly during the summer seasons (Figure 4a for SH and Figure 4c for NH), high variabilities are seen in the transitional zones between the tropical and polar gyres. SDs in the Arctic and Subarctic Oceans are significantly high during

the boreal summer (Figure 4c) but remain low in other seasons when sea ice coverage dominates. In the summer, SSTs are strongly influenced by the continental climate and modulated by sea ice melting in the coastal regions, and also influenced by meandering of the Kuroshio and Gulf Stream in the central North Pacific and northwestern North Atlantic. Another reason for the high variability in the Arctic SSTs is the fast warming rate in the Arctic near-surface air temperature, also known as the Arctic amplification (Rantanen et al., 2022), which can influence the SSTs and contribute to the increasing number of extreme events such as marine heatwaves (Carvalho & Wang, 2020; Huang et al., 2021b). Meanwhile, it should be noted here that a change in the algorithm for ice water temperature in DOISST v2.1, which will be discussed later in section 4.1, may also have contributed to the already high variations in the near-polar regions. However, this should not alter the conclusion since the similar high variability in the Arctic Ocean also appeared in the 1982–2011 climatology period, which was not affected by the algorithm change. It is also worth noting that since its creation, DOISST has experienced several changes in algorithm and input data. Although during the changes, SST means were bias-corrected, SST variances in time and space may be affected. For instance, Zhu et al. (2022) examined the mesoscale SST variability in DOISST over the western boundary currents and detected an enhancement after 2007. The study attributed the cause to the change of satellite AVHRR instrument in 2007.

3.2 | Secondary climatological parameters

Figure 5 exhibits the annual count parameter for four criteria of SST: ≥20°C, ≥30°C, <0°C and <15°C. Similar to the SST means, the SST counts are also zonally distributed in the midlatitudes with high meridional gradients. Almost year-round, daily SSTs are above 20°C in the tropical zones (Figure 5a). The pattern for SST < 15°C (Figure 5d) is similar to that for SST ≥ 20°C but in a reversed pattern with the tropical zones rarely below 15°C. This is because between the Tropics and extratropics the isotherms are very dense as shown in Figure 3 and thus the 15 and 20°C isotherms are not much separated from each other. Days with SST ≥ 30°C (Figure 5b) are mainly seen in the tropical oceans: in the Indian Ocean, the coverage is from its north boundary to the south as far as the southern tip of Madagascar at nearly 30°S; in both the Pacific and Atlantic Oceans, the coverages are between about 20°S and 35°N in the west but gradually decrease eastward. Long periods of days (around 120) with SST ≥ 30°C are seen in small ranges of the coastal sea of northern Sumatra Island and off the north Australian coast in the Timor Sea and Gulf of Carpentaria, and in a relatively larger area in the Bismarck and Solomon Seas. The highest number of days (around 180) with SST ≥ 30°C is seen in the Persian Gulf and the Red Sea. As the largest lake on earth and also located outside of the tropical zone, the Caspian Sea is unique in that there are days with temperatures exceeding 30°C in its northern and southern water body in a normal year. Long periods of days (over 180) with sub-zero SSTs are primarily seen in the Arctic (including the Hudson Bay) and Southern Oceans. Outside the polar regions, shorter periods of days (less than 60) with sub-zero SSTs are also observed in the southernmost water of the Indian, Pacific and Atlantic Oceans, west coastal seas of the North Pacific and North Atlantic Oceans reaching as far south as 45°N. Year-round (over 360 days) sub-zero SSTs are found in the coastal seas of Antarctica particularly the Ross and Weddell Seas, and most of the Arctic Ocean except the marginal seas, particularly the Barents and Kara Seas.

The 1991–2020 annual SST extremes, as displayed in Figure 6, are a consequence of both large-scale seasonal variations and small-scale perturbations in SST. First, the SST seasonality plays a crucial role in the SST extremes as suggested by the geographically coherent patterns shown on the plots, which resemble those of the SST means. The global SSTs are bounded by the ocean water freezing SST of −1.8°C at the lower end and largely by the warm pool SSTs exceeding 28°C at the upper end. On the annual highest SST plot (Figure 6a), the tropical ocean is predominantly covered by SSTs exceeding 28°C. In connection with the seasonal-daily SST patterns of Figure 2, we can see that the coverage of the 28°C isotherm on the highest SST plot is practically a combination of all the seasonal warm pool coverage, representing the probable maximum range of the tropical ocean warm pool. On the annual lowest SST plot (Figure 6b), freezing SSTs are seen in nearly the entire Southern Ocean, Arctic and Subarctic Oceans, demonstrating the probable maximum extent of sea ice coverage. In the Tropics, while the highest SST features the warm pool, the lowest SST clearly displays the Pacific equatorial cold tongue of its probable maximum range, as outlined by the 24°C isotherm. Second, localized small-scale perturbations in the extreme SSTs are reflected by the rough isotherms and relatively smaller isolated isothermal areas. The latter are particularly obvious on the highest SST plot for SSTs exceeding 32°C in the Arabian Sea, Bay of Bengal, north of Australia in the Timor and Arafura Seas, and the Gulf of Carpentaria, the western Pacific across Southeast Asia, the eastern Pacific along the coast of Latin America north of the equator. These small-scale SST extremes can be

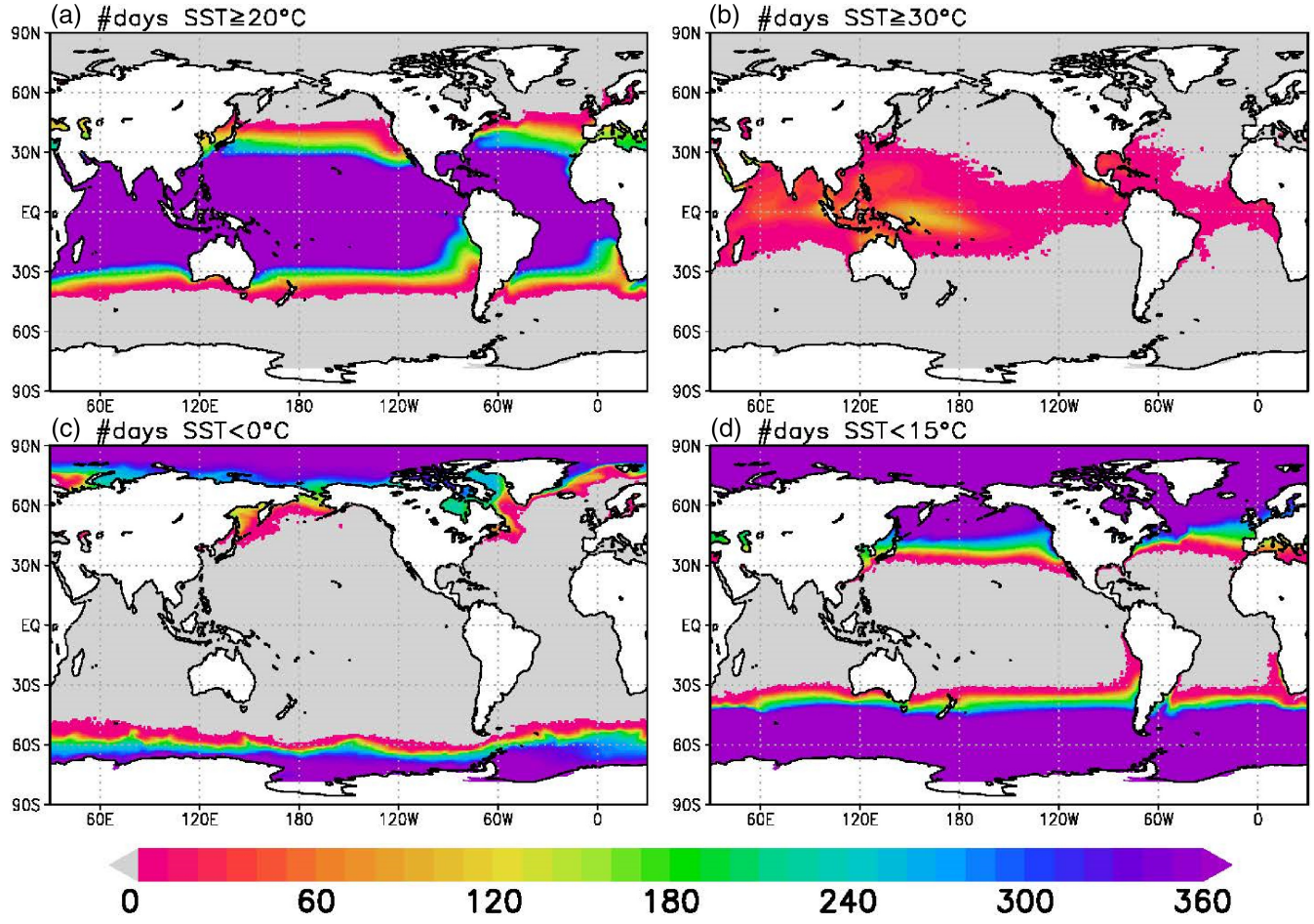

FIGURE 5 Annual normal SST count (units: days) for the number of days with SST (a) ≥20°C, (b) ≥30°C, (c) <0°C and (d) <15°C. [Colour figure can be viewed at wileyonlinelibrary.com]

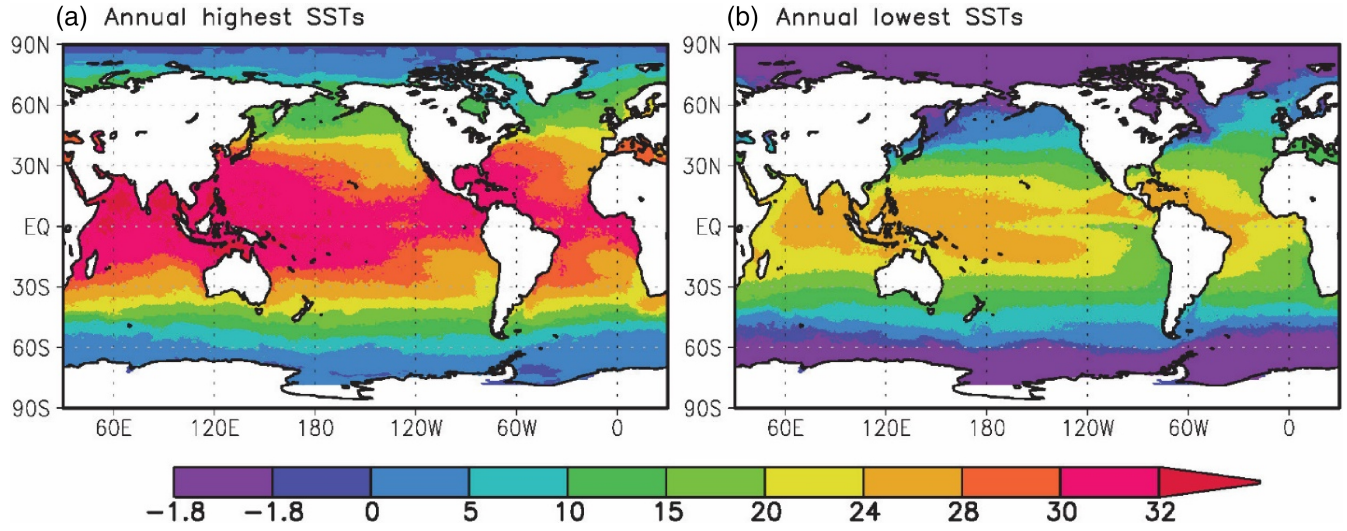

FIGURE 6 Annual SST extremes (units: °C) during 1991–2020: (a) highest SSTs and (b) lowest SSTs. [Colour figure can be viewed at wileyonlinelibrary.com]

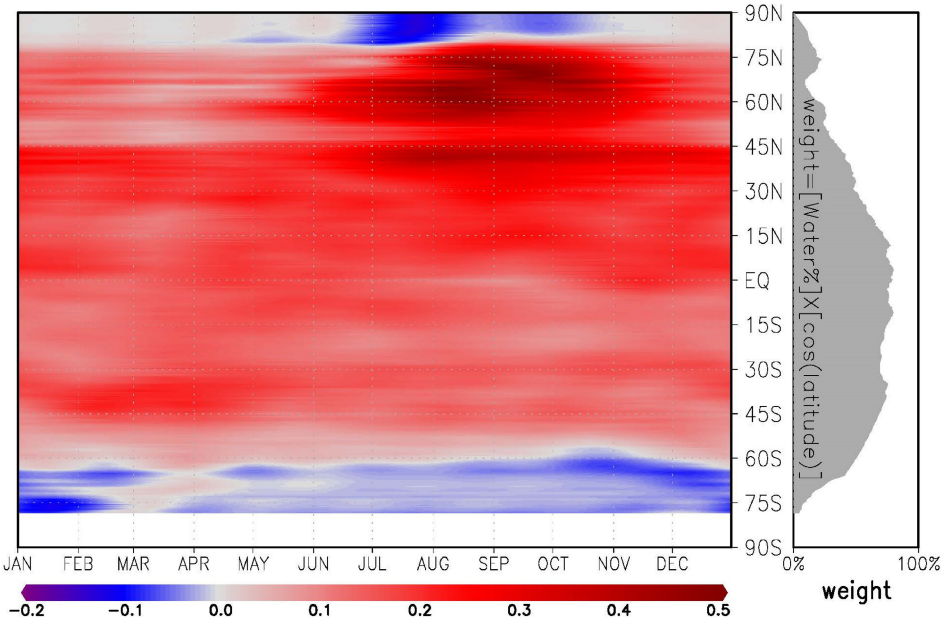

FIGURE 7 Difference between the 1991–2020 and 1982–2011 zonal mean daily SST climatologies (units: °C). The left panel is the time series of 1991–2020 minus 1982–2011. The right panel is the weight each latitude contributes to the global mean. The weight is computed by the product of the water portion and the cosine of the latitude. [Colour figure can be viewed at wileyonlinelibrary.com]

associated with marine extreme events including cold-spells and heatwaves (Huang et al., 2021b; Schlegel et al., 2021).

4 | INTERCOMPARISON BETWEEN THE 1991–2020 AND 1982–2011 CLIMATOLOGIES

To evaluate the changes in the SST's mean state, the 1991–2020 SST normals are compared with the 1982–2011 SST climatology. In addition to the daily SST mean climatology computed by Banzon et al. (2014), the other parameters in the current normals suite were also computed for the 1982–2011 period in order to perform a thorough comparison. In the following, the comparison results for selected mean and count parameters are presented. For description convenience, the term "climatology" is also used for the 1991–2020 normals during the comparison.

4.1 | Comparison of zonal mean SST climatologies

With the dominant latitudinal distribution pattern in the SST mean climatology, we use zonal mean to study the temporal evolution of global SST in a time-longitude space. The left panel of Figure 7 shows the difference of the two zonal mean daily SST climatologies (current minus previous) for Julian days 1–365. Obviously, the 1991–2020 climatology is warmer than the 1982–2011 climatology in all latitude bands except the northern Arctic and Southern Oceans during certain months. The highest warming magnitude (>0.5°C) is in the midlatitude to high latitude of NH during the boreal summer into fall. Except in a short period between late February and April (austral summer to fall), the Southern Ocean exhibits a large-scale cooling effect, especially between October and late February (austral spring to summer, between −0.10°C and −0.05°C). The northern Arctic Ocean shows a relatively stronger cooling effect from boreal spring to early fall, particularly in July and August (boreal summer, between −0.12°C and −0.05°C). Although the data suggest that the Arctic and Southern Ocean strongly cooled during the warm seasons, this is likely due to an algorithm change in DOISST which will be discussed later in this section. It should be noted that the contribution of each zonal mean to the global mean depends on its contribution weight, that is, the product of water portion and the cosine of the latitude, which is shown in the right panel of Figure 7. By the weight curve, we can see that the cooling in the two polar oceans only makes a very small contribution to the overall global SST mean or trend.

With global warming happening, the cooling phenomena shown in the climatologies in the northern Arctic and Southern Oceans are of great interest. A further investigation is carried out on the time series of zonal mean SST anomalies during 1982–2020, which covers both climatology periods. Since the DOISST is a satellite and in situ blended product, which is sensitive to SST retrieval algorithms, the in situ-based ERSST version 5 is also used here for verification purpose. Figure 8 displays the 1982–2020 time series of zonal mean monthly SST anomalies (base period 1982–2020) for both DOISST and

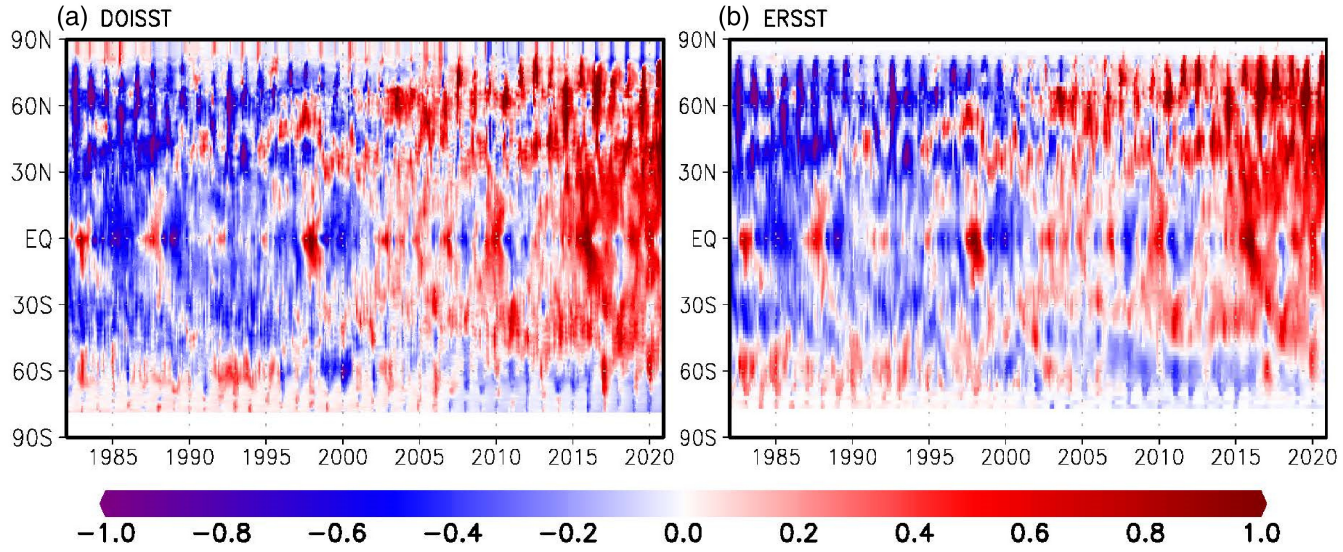

FIGURE 8 Zonal mean monthly SST anomalies (units: °C) during 1982–2020 for (a) DOISST version 2.1 and (b) ERSST version 5. [Colour figure can be viewed at wileyonlinelibrary.com]

ERSST. It is seen from the figure that the variations of the two products are consistent in general but differences in recent years appear in the two polar oceans where the seasonal cooling in DOISST is nearly unseen in ERSST. Our investigation concluded that this systematic seasonal cooling in the DOISST (Figure 8a) is caused by an algorithm change for proxy SST from ice concentration in DOISST version 2.1 (Huang et al., 2021a), which was to correct the warm bias found in version 2.0 (Banzon et al., 2020; Castro et al., 2016). The algorithm update for warm-bias correction has only been applied to the version 2.1 portion of the DOISST data starting in 2016 and thus in regions where seasonal ice presents a warm bias exhibited in the time series before 2016. For DOISST (Figure 8a), during the post-2015 summer months when ice-water mixture appears, negative SST anomalies are seen in both polar oceans, with greater prominence in the northern Arctic Ocean. Consequently, as seen from Figure 7, the DOISST-based 1991–2020 climatology appears to be colder than the 1982–2011 climatology in the northern Arctic Ocean during July–October and in the Southern Ocean during December–February. In contrast, in the ERSST time series (Figure 8b), the polar region seasonal cooling exhibited in DOISST is absent in the northern Arctic Ocean and only slightly seen in the Southern Ocean. With these considerations, the climatology cooling in the northern Arctic Ocean shown in the DOISST-based 1991–2020 normals is questionable. However, in the Southern Ocean, the overall cooling is consistent in the DOISST and ERSST, confirming that a cooling trend exists in the Southern Ocean. On the other hand, a study using ocean profile observations during 1992–2017 found that despite the cooling trend observed in the near-surface water of the Southern Ocean, the subsurface to a depth of up to 800 m is characterized by a warming trend (Auger et al., 2021).

4.2 | Comparison of SST spatial patterns

Figure 9 shows the difference between the 1991–2020 and 1982–2011 seasonal SST climatologies. Overall, the difference is more pronounced during the boreal summer (Figure 9c) and fall (Figure 9d). In Figure 9c, the geographical sources of the highest warming rate shown in Figure 7 can be identified as areas including the southern Arctic and Subarctic Oceans, midlatitude North Pacific and midlatitude western North Atlantic Oceans.

Among the large-scale warming trends in the Tropics and extratropics, the cooling blobs appearing in the midlatitude North Atlantic, tropical South Atlantic and eastern tropical South Pacific Oceans are outstanding (Figure 9). The North Atlantic cooling, located to the south of Greenland, is clear during the boreal winter, spring and summer seasons. It is part of the North Atlantic warming hole that has been widely reported and analysed in the past and was commonly believed to be associated with a decline of the Atlantic meridional overturning circulation (Drijfhout et al., 2012; Huang et al., 2017). The cooling in the two tropical oceans is especially strong during the austral spring OND (Figure 9d). As the two climatologies have a common period 1991–2011, their difference may be either simply due to a non-trend-related difference between the two ending periods 2012–2020 and 1982–1990, or a result of a long-term trend during the whole period 1982–2020. For

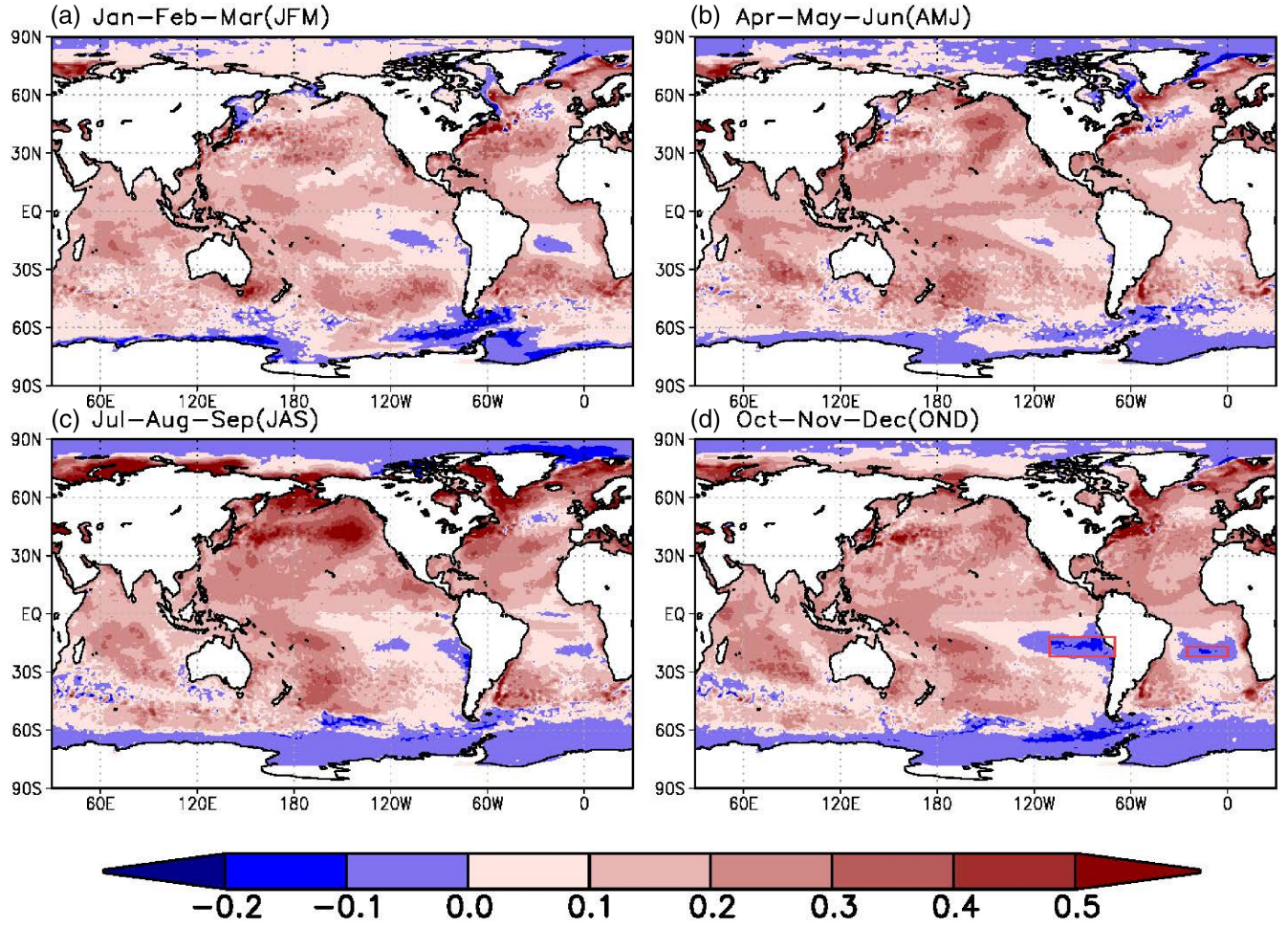

FIGURE 9 Seasonal SST climatology (units: °C) difference between 1991–2020 and 1982–2011. (a) January, February and March (JFM); (b) April, May and June (AMJ); (c) July, August and September (JAS); and (d) October, November and December (OND). The two red line box areas on panel d are used to investigate the SST trends. [Colour figure can be viewed at wileyonlinelibrary.com]

further investigation, a box area is selected within each cooling region during OND, as shown in Figure 9d. Then, areal mean OND average SST anomalies during 1982–2020 are computed for each box and trend analyses are conducted on the time series. For the Atlantic box, the trend is insignificant ($p > 0.05$) for the whole period 1982–2020 and even slightly positive for the current climatology period 1991–2020. Meanwhile, for the Pacific box off the Peruvian and Chilean coasts, the trend for 1982–2020 is statistically significant at $p < 0.05$, indicating the OND SST cooling in the climatologies is due to a persistent SST decreasing trend in this area.

To analyse the mechanism for the cooling trend in the eastern tropical South Pacific, we employ the 10 m meridional component of the wind (v-wind) from the ERA5 to examine the wind–SST relationship. Our analysis shows that the OND SST is closely associated with the previous season (JAS) v-wind. First, as exhibited in the upper panel of Figure 10, the trends of JAS v-wind during 1982–2020 are computed at each ocean grid within the box area 95°–70°W and 35°–5°S. This result shows that the eastern tropical South Pacific is dominated by increased v-wind with the strongest trends in the east portion between about 35°–15°S. Then, the 1982–2020 time series of the box areal mean JAS v-wind is shown in the lower panel of Figure 10, together with the time series of areal mean OND SST anomalies in the Pacific box defined in Figure 9d. Both the wind and SST have significant ($p < 0.05$) trends but in opposite signs. They are also significantly (at the 99% level) correlated with $r = -0.56$ for the original time series and $r = -0.49$ for the detrended time series. The inverse relationship between v-wind and SST in both trends and variations suggests that between the two parameters there exists a cause-and-effect relationship, in which the increased v-wind in JAS (austral winter) leads to intensified upwellings, resulting in an ocean cooling trend in the following season OND (austral

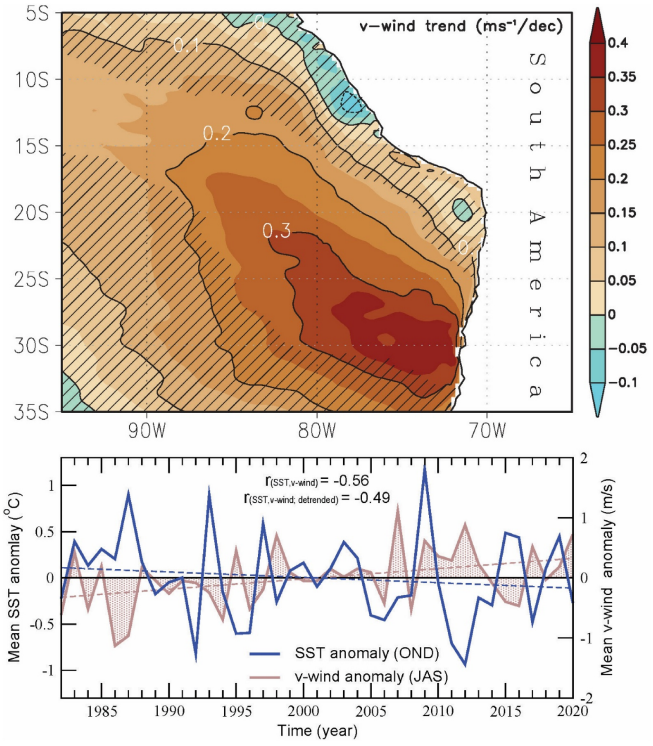

FIGURE 10 Surface wind and SST in the tropical eastern South Pacific: (upper panel) trends (units: $m \cdot s^{-1} \cdot decade^{-1}$) of the July–August–September (JAS) mean meridional component of the 10 m wind (v-wind) anomalies during 1982–2020 on 0.25 × 0.25 grids. The trends in non-hatched grids are significant with $p < 0.05$; (lower panel) 1982–2020 seasonal time series of the areal mean JAS v-wind anomalies from the upper panel box and October–November–December (OND) SST anomalies from the tropical eastern South Pacific box shown in Figure 9d. The dashed lines are the linear trend lines for v-wind and SST. Both trends are significant with $p < 0.05$. The correlation coefficient between SST and v-wind is −0.56 for the original time series and −0.49 for detrended time series, both are significant at the 99% level. [Colour figure can be viewed at wileyonlinelibrary.com]

spring). These results are consistent with an earlier study of Zou and Xi (2021) based on buoy observations during 1992–2018.

4.3 | Comparison of the Indo-Pacific warm pool

The IPWP is traditionally defined by the area with annual or seasonal average SSTs exceeding 28°C (Roxy et al., 2019; Wyrtki, 1989). In this study, we use the count parameter from the two climatologies as an alternative metric to define IPWP and analyse its changes between the 1991–2020 and 1982–2011 climatologies. The criterion is the annual number of days with SST ≥ 28°C (ND28; units: day).

First, the intensity of the warm pool, measured by the magnitude of ND28, is compared between the two climatologies by using a relaxed warm pool definition. In Figure 11, the colour shading marks the areas with ND28 ≥ 182.5 (i.e., climatologically at least half a year with SST ≥ 28°C) in the 1982–2011 climatology and the colour scale represents the changes from the 1982–2011 to 1991–2020 climatology. In the Indo-Pacific Ocean, the warm pool coverage spans a west–east elongated area from about 50°E in the western Indian Ocean, passing Southeast Asia, to about 140°W in the eastern Pacific Ocean. Straddling the Equator, the region mostly situates between 10°S and 20°N west of 160°E, and then extends slightly southward between about 18°S and 10°N. Between the two climatologies, ND28 increased in all areas from a few days in the inner part to over 20 days in the outer part of the domain, indicating an enhancement of the warm pool. Second, we select ND28 ≥ 300 (i.e., climatologically at least 300 days in a year with SST ≥ 28°C) as a stricter definition for IPWP to study its spatial coverage change. In Figure 11, the white and blue contours, respectively, enclose the IPWP ranges in 1982–2011 and 1991–2020. The figure shows that IPWP expanded in all directions, particularly north of the Equator. From 1982–2011 to 1991–2020, the spatial coverage of IPWP as defined by ND28 ≥ 300 increased by 33%, from 16.6 to 22.1 million km^2.

4.4 | Comparison of global mean SSTs

The two climatologies are compared by the global mean SSTs on annual, monthly and daily scales. As shown in Figure 12, from 1982–2011 to 1991–2020, warming is seen at all time scales and is the greatest during the boreal summer and the least during the boreal winter. In connection with Figures 7 and 9, the strong boreal summer warming is mainly contributed from the midlatitude and high-latitude oceans in NH. On annual average, the 1991–2020 climatology was warmer than the 1982–2011 climatology by 0.14°C. In the four consecutive months in boreal summer into fall (July–October), the monthly warming rate was above the annual average, while in 3 months, which are in the transition seasons of boreal spring (April and June) and fall (November), the monthly warming rate was equal to that of the annual average.

5 | SUMMARY AND DISCUSSIONS

The 1991–2020 climatological standard normals for sea surface temperature (SST) were computed based on the gridded daily mean SST product DOISST. This suite of

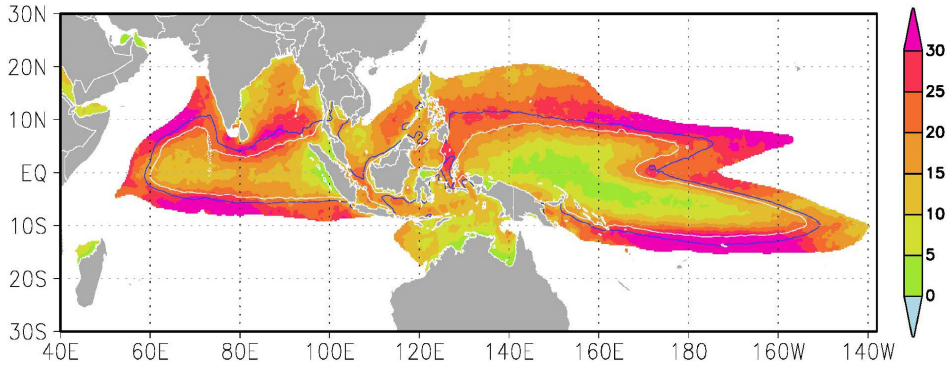

FIGURE 11 Comparison of the 1982–2011 and 1991–2020 Indo-Pacific warm pools (IPWPs) based on annual count parameter of number of days with SST ≥ 28°C (ND28; units: days). The colour shading area is the coverage of ND28 ≥ 182.5 in the 1982–2011 climatology and the colour scale represents the ND28 difference between the two climatologies (1991–2020 minus 1982–2011). The ND28 ≥ 300 coverages in 1982–2011 and 1991–2020 are, respectively, the areas enclosed by the white and blue curves. [Colour figure can be viewed at wileyonlinelibrary.com]

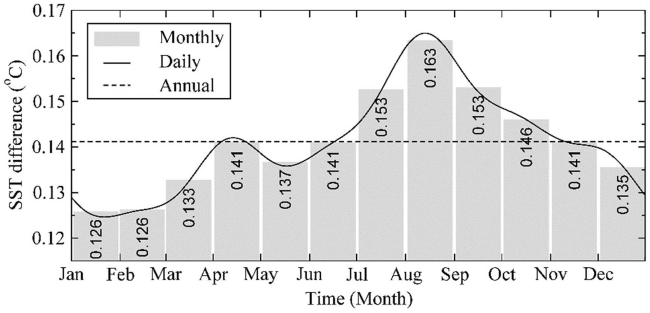

FIGURE 12 Global mean SST difference between the two climatologies (1991–2020 minus 1982–2011) at annual, monthly and daily scales.

SST normals contains the principal and secondary climatological parameters. The principal category includes SST mean parameters on daily, monthly, seasonal and annual time scales; the secondary includes SST count and extreme parameters on monthly, seasonal and annual time scales. Standard deviations (SDs) were also calculated for the SSTs during the averaging period. The spatial resolution of the product is 0.25° latitude–longitude, the same as that of the underlying input data DOISST.

In general, SSTs are higher in the Tropics and gradually decrease poleward. In the tropical Pacific and Atlantic Oceans, SSTs are higher in the west and decrease eastward. The Indo-Pacific Oceans are featured by the tropical warm pool temperature of SST ≥ 28°C and the eastern tropical Pacific Ocean is characterized by the cold tongue temperature of SST ≤ 24°C. The polar oceans of 60° poleward are dominated by sub-zero to freezing-point SSTs. Spatial variations or meridional gradients are low in the low latitudes but significantly high in the mid-latitude to high latitude. During the averaging period 1991–2020, the SST SDs as assessed against the normal SST means are generally low (<1.0°C for daily) but can be obviously high (>1.5°C for daily) in the frontal zones mostly associated with ocean currents. For the secondary parameters (count and extreme), their spatial distribution patterns are similar to those of the SST means with low spatial variations in the low latitudes and zonal distribution with high meridional gradients in the midlatitudes. The patterns of SST extremes are primarily determined by the large-scale seasonal variations of SST with the probable maximum extents of the warm pool and the cold tongue in the Tropics, respectively. For the extreme SST, localized small-scale SST perturbations are also seen globally, particularly in the Tropics for the highest SST. They are associated with marine extreme events such as marine cold-spells and heatwaves.

The 1991–2020 SST normals were compared with the 1982–2011 SST climatology. The difference of the mean SSTs shows an overall warming but seasonal cooling was found in the North and tropical Atlantic Ocean, northern Arctic Ocean, Southern Ocean and eastern tropical South Pacific Ocean. The cooling was significant except for that in the tropical Atlantic. Attribution analysis was then conducted for the cooling phenomena in the climatologies. In the North Atlantic, the cooling is associated with the warming hole. In the ice covered regions of the Arctic and the Antarctic, the DOISST v2.1 has an algorithm change for proxy SST from ice concentration to correct the warm bias found in its previous version. The new algorithm is applied only to the post-2015 data and consequently a cooling artefact is detected due to the warm bias over 1982–2015. The impact on the trend is severe in the northern Arctic Ocean but limited in the Southern Ocean, where the existence of a large-scale cooling is verified by other data sets including the ERSST.

It needs to be noted that this algorithm change also has an impact on other parameters, among which, the count for freezing point SST is affected the most and thus should be used with caution. Nonetheless, while the algorithm inconsistency issue will not be resolved until the next major version update in the underlying input dataset, this algorithm-induced warm bias over 1982–2015 has very minor influence on global mean due to the relatively minimal weight from each region. Trend and correlation analysis of SST and wind data from reanalysis during 1982–2020 confirms that the cooling in the eastern tropical South Pacific is associated with the intensification of southerlies in the region. Furthermore, by analysing both buoy observation and model simulation, Zou and Xi (2021) pointed out that the increased southerlies along the west shores of South America were due to the eastward migration of the Southeast Pacific subtropical anticyclone which was blocked by the Andes Mountains.

Meanwhile, the enhanced warming (in the west)/cooling (in the east) contrast across the tropical Pacific has significant impacts on the global climate system and thus has received wide interests on its attributions and variations. Study shows that this phenomenon may be associated with the regime shift occurred in 1999/2000 that featured a decrease in the variability and an increase in the frequency of ENSO (Hu et al., 2020). However, as evidenced by the divergence among observations and model simulations, there are uncertainties in determining whether the strengthening zonal SST gradient is due to human activity, natural variability, or both, or may be due to flaws in observations (Lee et al., 2022).

The Indo-Pacific warm pool (IPWP) was examined by using the count parameter of annual number of days with SST $\geq 28^{\circ}C$ in the climatologies. The result shows that IPWP has strengthened in both intensity and coverage since the last climatology period. Using the criterion of annually at least 300 days with SST $\geq 28^{\circ}C$ for IPWP, its spatial coverage increased 33% from 1982–2011 to 1991–2020. The IPWP's strengthening may be partially associated with ENSO's regime shift happened in 1999/2000 (Hu et al., 2020). Meanwhile, the analysis of Roxy et al. (2019) showed that the IPWP has been expanding continuously during 1900–2018 and at an accelerated rate in the last few decades. The IPWP affects the global system through supporting tropical convection. However, Leung et al. (2022) indicated that the IPWP expansion differs from the deep convection favouring pool area change and may not reflect the direct impacts of Indo-Pacific warming on the climate system.

The comparison of global mean SST between the two climatologies shows that global warming is happening at all time scales, from annual, to monthly, and to daily. The warming rate is the highest during boreal summer and the lowest during boreal winter. On an annual average, the global mean SST of 1991–2020 is higher than that of 1982–2011 by 0.14°C, which is equivalent to a warming rate of $0.16^{\circ}C \cdot decade^{-1}$. This doubles the 1901–2020 long-term average trend of $0.08^{\circ}C \cdot decade^{-1}$ (NOAA National Centers for Environmental Information, 2023). In fact, the difference between the two climatologies stems from their non-overlapping periods. For the global mean SST, of the 9 years in the last period 2012–2020, seven were ranked in the top 10 warmest years during the 1901–2020 period (NOAA National Centers for Environmental Information, 2023).

Some studies argued that the 30-year period is not always the best choice for climate normals and the optimal period for temperatures is often substantially shorter than 30 years (Huang et al., 1996; Wilks, 2013; WMO, 2018). In this work, to satisfy users' needs, we also computed the SST normals for the most recent 15-year period 2006–2020 as a supplemental SST normals product.

AUTHOR CONTRIBUTIONS

Xungang Yin: Conceptualization; methodology; software; investigation; writing – original draft; data curation; visualization; formal analysis. **Boyin Huang:** Investigation; validation; writing – review and editing; data curation; software; methodology; formal analysis; conceptualization. **James A. Carton:** Writing – review and editing; investigation. **Ligang Chen:** Investigation; writing – review and editing. **Garrett Graham:** Investigation; writing – review and editing. **Chunying Liu:** Investigation; writing – review and editing. **Thomas Smith:** Investigation; writing – review and editing. **Huai-Min Zhang:** Investigation; supervision; project administration; writing – review and editing; funding acquisition.

ACKNOWLEDGEMENTS

The authors thank the two anonymous reviewers for their comments that have greatly improved our manuscript. James A. Carton and Ligang Chen were supported by the NOAA Climate Program Office (NA20OAR4310339). The graphics were generated using Grid Analysis and Display System (GrADS) and GRaphing, Advanced Computation and Exploration of data (GRACE).

DATA AVAILABILITY STATEMENT

The data that support the findings of this study are openly available: DOISST from NCEI at https://www.ncei.noaa.gov/products/optimum-interpolation-sst; ERSST from NCEI at https://www.ncei.noaa.gov/products/extended-reconstructed-sst; ERA5 from ECMWF at https://www.ecmwf.int/en/forecasts/datasets/reanalysis-datasets/era5. The SST climate normals data sets and the program codes

used for generating the data sets are openly available at https://www.ncei.noaa.gov/pub/data/cmb/ersst/v5/2023.sst.normals/.

ORCID

Xungang Yin https://orcid.org/0000-0002-3775-6587

REFERENCES

Arguez, A. & Applequist, S. (2013) A harmonic approach for calculating daily temperature normals constrained by homogenized monthly temperature normals. *Journal of Atmospheric and Oceanic Technology*, 30, 1259–1265. Available from: https://doi.org/10.1175/JTECH-D-12-00195.1

Auger, M., Morrow, R., Kestenare, E., Sallée, J.-B. & Cowley, R. (2021) Southern Ocean in-situ temperature trends over 25 years emerge from interannual variability. *Nature Communications*, 12, 514. Available from: https://doi.org/10.1038/s41467-020-20781-1

Banzon, V., Smith, T.M., Steele, M., Huang, B. & Zhang, H.-M. (2020) Improved estimation of proxy sea surface temperature in the Arctic. *Journal of Atmospheric and Oceanic Technology*, 37, 341–349. Available from: https://doi.org/10.1175/JTECH-D-19-0177.1

Banzon, V.F., Reynolds, R.W., Stokes, D. & Xue, Y. (2014) A 1/4°-spatial-resolution daily sea surface temperature climatology based on a blended satellite and in situ analysis. *Journal of Climate*, 27, 8221–8228. Available from: https://doi.org/10.1175/JCLI-D-14-00293.1

Bottomley, M., Folland, C.K., Hsiung, J., Newell, R.E. & Parker, D.E. (1990) *Global ocean surface temperature atlas (GOSTA)*. London: Joint Meteorological Office/Massachusetts Institute of Technology project, HMSO. Technical report, 24 pp. and 313 plates.

Carvalho, K. & Wang, S. (2020) Sea surface temperature variability in the Arctic Ocean and its marginal seas in a changing climate: patterns and mechanisms. *Global and Planetary Change*, 193, 103265. Available from: https://doi.org/10.1016/j.gloplacha.2020.103265

Castro, S.L., Wick, G.A. & Steele, M. (2016) Validation of satellite sea surface temperature analyses in the Beaufort Sea using UpTempO buoys. *Remote Sensing of Environment*, 187, 458–475. Available from: https://doi.org/10.1016/j.rse.2016.10.035

Dinsmore, R.P. (1996) Alpha, bravo, Charlie... ocean weather ships 1940–1980. *Oceanus Fall/Winter*, 39, 9–10. Available from: http://www.whoi.edu/oceanus/feature/alpha-bravo-charlie/

Drijfhout, S., van Oldenborgh, G.J. & Cimatoribus, A. (2012) Is a decline of AMOC causing the warming hole above the North Atlantic in observed and modeled warming patterns? *Journal of Climate*, 25, 8373–8379. Available from: https://doi.org/10.1175/JCLI-D-12-00490.1

Emery, W.J. (2015) Air-sea interactions: sea surface temperature. In: North, G.R., Pyle, J. & Zhang, F. (Eds.) *Encyclopedia of atmospheric sciences*, 2nd edition. Oxford, UK: Elsevier, pp. 136–143.

Epstein, E.S. (1991) Determining the optimum number of harmonies to represent normals based on multiyear data. *Journal of Climate*, 4, 1047–1051. Available from: https://doi.org/10.1175/1520-0442(1991)004<1047:DTONOH>2.0.CO;2

Hersbach, H., Bell, B., Berrisford, P., Hirahara, S., Horányi, A., Muñoz-Sabater, J. et al. (2020) The ERA5 global reanalysis. *Quarterly Journal of the Royal Meteorological Society*, 146, 1999–2049. Available from: https://doi.org/10.1002/qj.3803

Hu, Z., Kumar, A., Huang, B., Zhu, J., L'Heureux, M., McPhaden, M.J. et al. (2020) The interdecadal shift of ENSO properties in 1999/2000: a review. *Journal of Climate*, 33, 4441–4462. Available from: https://doi.org/10.1175/JCLI-D-19-0316.1

Huang, B., Liu, C., Banzon, V., Freeman, E., Graham, G., Hankins, B. et al. (2021a) Improvements of the daily optimum interpolation sea surface temperature (DOISST) version 2.1. *Journal of Climate*, 34, 2923–2939. Available from: https://doi.org/10.1175/JCLI-D-20-0166.1

Huang, B., Thorne, P.W., Banzon, V.F., Boyer, T., Chepurin, G., Lawrimore, J.H. et al. (2017) Extended Reconstructed Sea Surface Temperature version 5 (ERSSTv5), upgrades, validations, and intercomparisons. *Journal of Climate*, 30, 8179–8205. Available from: https://doi.org/10.1175/JCLI-D-16-0836.1

Huang, B., Wang, Z., Yin, X., Arguez, A., Graham, G., Liu, C. et al. (2021b) Prolonged marine heatwaves in the Arctic: 1982–2020. *Geophysical Research Letters*, 48, e2021GL095590. Available from: https://doi.org/10.1029/2021GL095590

Huang, B., Yin, X., Carton, J.A., Chen, L., Graham, G., Liu, C. et al. (2023) Understanding differences in sea surface temperature intercomparisons. *Journal of Atmospheric and Oceanic Technology*, 40, 455–473. Available from: https://doi.org/10.1175/JTECH-D-22-0081.1

Huang, J., VandenDool, H.M. & Barnston, A.G. (1996) Long-lead seasonal temperature prediction using optimal climate normals. *Journal of Climate*, 9, 809–817. Available from: https://doi.org/10.1175/1520-0442(1996)009%3C0809:LLSTPU%3E2.0.CO;2

Kawai, Y. & Wada, A. (2007) Diurnal sea surface temperature variation and its impact on the atmosphere and ocean: a review. *Journal of Oceanography*, 63, 721–744. Available from: https://doi.org/10.1007/s10872-007-0063-0

Lee, S., L'Heureux, M., Wittenberg, A.T., Richard, S., O'Gorman, P.A. & Johnson, N.C. (2022) On the future zonal contrasts of equatorial Pacific climate: perspectives from observations, simulations, and theories. *npj Climate and Atmospheric Science*, 5, 82. Available from: https://doi.org/10.1038/s41612-022-00301-2

Leung, J.C.-H., Zhang, B., Gan, Q., Wang, L., Qian, W. & Hu, Z.-Z. (2022) Differential expansion speeds of Indo-Pacific warm pool and deep convection favoring pool under greenhouse warming. *npj Climate and Atmospheric Science*, 5, 97. Available from: https://doi.org/10.1038/s41612-022-00315-w

Minnett, P.J., Alvera-Azcárate, A., Chin, T.M., Corlett, G.K., Gentemann, C.L., Karagali, I. et al. (2019) Half a century of satellite remote sensing of sea-surface temperature. *Remote Sensing of Environment*, 233, 111366. Available from: https://doi.org/10.1016/j.rse.2019.111366

NOAA National Centers for Environmental Information. (2022a) U.S. climate normals. Available from: https://www.ncei.noaa.gov/products/land-based-station/us-climate-normals [Accessed 5th March 2023]

NOAA National Centers for Environmental Information. (2022b) World ocean atlas. Available from: https://www.ncei.noaa.gov/products/world-ocean-atlas [Accessed 5th March 2023]

NOAA National Centers for Environmental Information. (2023) Climate at a glance: global time series. Available from: https://www.ncei.noaa.gov/access/monitoring/climate-at-a-glance/global/time-series [Accessed 5th March 2023]

Peng, G., Arguez, A., Meier, W.N., Vamborg, F., Crouch, J. & Jones, P. (2019) Sea ice climate normals for seasonal ice monitoring of Arctic and sub-regions. *Data*, 4, 122. Available from: https://doi.org/10.3390/data4030122

Rantanen, M., Karpechko, A.Y., Lipponen, A., Nordling, K., Hyvärinen, O., Ruosteenoja, K. et al. (2022) The Arctic has warmed nearly four times faster than the globe since 1979. *Communications Earth & Environment*, 3, 168. Available from: https://doi.org/10.1038/s43247-022-00498-3

Reynolds, R.W., Smith, T.M., Liu, C., Chelton, D.B., Casey, K.S. & Schlax, M.G. (2007) Daily high-resolution blended analyses for sea surface temperature. *Journal of Climate*, 20, 5473–5496. Available from: https://doi.org/10.1175/2007JCLI1824.1

Roxy, M.K., Dasgupta, P., McPhaden, M.J., Suematsu, T., Zhang, C. & Kim, D. (2019) Twofold expansion of the Indo-Pacific warm pool warps the MJO life cycle. *Nature*, 575, 647–651. Available from: https://doi.org/10.1038/s41586-019-1764-4

Schlegel, R.W., Darmaraki, S., Benthuysen, J.A., Filbee-Dexter, K. & Oliver, E.C.J. (2021) Marine cold-spells. *Progress in Oceanography*, 198, 102684. Available from: https://doi.org/10.1016/j.pocean.2021.102684

Shea, D.J. (1986) *Climatological atlas: 1950–1979 surface air temperature, precipitation, sea-level pressure, and sea-surface temperature (45°S–90°N)*. NCAR/TN-269+STR. Bolder, Colorado, USA: University Corporation for Atmospheric Research. Available from: https://doi.org/10.5065/D6G73BNG

Shea, D.J., Trenberth, K.E. & Reynolds, R.W. (1992) A global monthly sea surface temperature climatology. *Journal of Climate*, 5, 987–1001. Available from: https://doi.org/10.1175/1520-0442(1992)005%3C0987:AGMSST%3E2.0.CO;2

Stuart-Menteth, A.C., Robinson, I.S. & Challenor, P.G. (2003) A global study of diurnal warming using satellite-derived sea surface temperature. *Journal of Geophysical Research*, 108, 3155. Available from: https://doi.org/10.1029/2002JC001534

Talley, L.D., Pickard, G.L., Emery, W.J. & Swift, J.H. (2011) *Descriptive physical oceanography: an introduction*, 6th edition. Boston, USA: Elsevier, 560 pp.

Taylor, A.H. & Stephens, J.A. (1980) Seasonal and year-to-year variations in surface salinity at the nine North-Atlantic Ocean weather stations. *Oceanologica Acta*, 3, 421–430.

Tveito, O.E. (2021) *Norwegian standard climate normals 1991–2020 the methodological approach*. Oslo: Meteorologisk Institutt. MET report 05/2021, 484 pp. Available from: https://www.met.no/publikasjoner/met-report/met-report-2021

von Storch, H. & Zwiers, F.W. (1999) *Statistical analysis in climate research*. Cambridge: Cambridge University Press.

Wang, K. & Clow, G.D. (2020) The diurnal temperature range in CMIP6 models: climatology, variability, and evolution. *Journal of Climate*, 33, 8261–8279. Available from: https://doi.org/10.1175/JCLI-D-19-0897.1

Wilks, D.S. (2006) *Statistical methods in the atmospheric sciences. International geophysics series*, Vol. 91, 2nd edition. Boston, USA: Academic Press, 627 pp.

Wilks, D.S. (2013) Projecting "Normals" in a nonstationary climate. *Journal of Applied Meteorology and Climatology*, 52, 289–302.

WMO. (2007) *The role of climatological normals in a changing climate*. Geneva: WMO. WMO-TD No. 1377, 130 pp. Available from: https://library.wmo.int/doc_num.php?explnum_id=4546

WMO. (2011) *Commission for climatology: over eighty years of service*. Geneva: WMO. WMO-No. 1079, 60 pp. Available from: https://library.wmo.int/doc_num.php?explnum_id=5116

WMO. (2015) *Seventeenth world meteorological congress*. Geneva: WMO. WMO-No. 1157, 708 pp. Available from: https://library.wmo.int/doc_num.php?explnum_id=3138

WMO. (2016) *Technical regulations, basic documents No. 2, Volume I—general meteorological standards and recommended practices*. Geneva: WMO. WMO-No. 49, 2019 edition, updated in 2021, 71 pp. Available from: https://library.wmo.int/doc_num.php?explnum_id=10955

WMO. (2017) *Guidelines on the calculation of climate normals*. Geneva: WMO. WMO No. 1203, 29 pp. Available from: https://library.wmo.int/doc_num.php?explnum_id=4166

WMO. (2018) *Guide to climatological practices*. Geneva: WMO. WMO-No. 100, 153 pp. Available from: https://library.wmo.int/doc_num.php?explnum_id=5541

Woodruff, S.D., Slutz, R.J., Jenne, R.L. & Steurer, P.M. (1987) A comprehensive ocean-atmosphere data set. *Bulletin of the American Meteorological Society*, 68, 1239–1250. Available from: https://doi.org/10.1175/1520-0477(1987)068%3C1239:ACOADS%3E2.0.CO;2

Wyrtki, K. (1989) Some thoughts about the West Pacific Warm Pool. In: *Proceedings of the Western Pacific international meeting and workshop on TOGA COARE*. Nouméa, New Caledonia: Institut Français de Recherche Scientifique Pour le Developpement en Cooperation, pp. 99–109. Available from: https://horizon.documentation.ird.fr/exl-doc/pleins_textes/divers21-04/26613.pdf

Yang, C., Leonelli, F.E., Marullo, S., Artale, V., Beggs, H., Nardelli, B.B. et al. (2021) Sea surface temperature intercomparison in the framework of the Copernicus Climate Change Service (C3S). *Journal of Climate*, 34, 5257–5283. Available from: https://doi.org/10.1175/JCLI-D-20-0793.1

Zhu, Y., Li, Y., Wang, F. & Lv, M. (2022) Weak mesoscale variability in the optimum interpolation sea surface temperature (OISST)-AVHRR-only version 2 data before 2007. *Remote Sensing*, 14(2), 409. Available from: https://doi.org/10.3390/rs14020409

Zou, Y., & Xi, X. (2021). An ongoing cooling in the eastern Pacific linked to eastward migrations of the Southeast Pacific Subtropical Anticyclone. *Environ. Res. Lett.* 16 034020. Avaliable from: https://doi.org/10.1088/1748-9326/abd819

How to cite this article: Yin, X., Huang, B., Carton, J. A., Chen, L., Graham, G., Liu, C., Smith, T., & Zhang, H.-M. (2024). The 1991–2020 sea surface temperature normals. *International Journal of Climatology*, *44*(2), 668–685. https://doi.org/10.1002/joc.8350